

Electrocrystallization of Hydroxyapatite and Its Dependence on Solution Conditions

Noam Eliaz* and T. M. Sridhar†

Biomaterials and Corrosion Laboratory, School of Mechanical Engineering, Tel-Aviv University, Ramat Aviv, Tel Aviv 69978, Israel

Received January 7, 2008; Revised Manuscript Received May 20, 2008

ABSTRACT: Electrocrystallization of hydroxyapatite (HAp) on titanium was achieved by cathodic polarization in solution containing calcium nitrate and ammonium dihydrogen phosphate. The composition and pH of the bath were found to significantly affect the nature and surface morphology of the deposit. The effect of bath temperature was also studied. X-ray diffraction tests and microscopic inspections confirmed the formation of well-crystallized HAp at $\text{pH}_0 = 6.0$ at any temperature between 70 and 95 °C, whereas, at $\text{pH}_0 = 4.2$, less-crystallized, thicker, and more porous coatings that contained traces of octacalcium phosphate were observed. The influence of potassium chloride and sodium nitrite on the composition and surface morphology of the deposit was also evaluated. A speciation–precipitation model was applied to better understand the effect of bath conditions. The standard enthalpy of activation was $\sim 40 \text{ kJ mol}^{-1}$, indicating that the reaction kinetics is controlled by the interfacial area. The corrosion resistance of the coatings was determined by open-circuit potential and cyclic potentiodynamic polarization measurements in a simulated body fluid. The samples coated at $\text{pH}_0 = 6.0$ exhibited nobler behavior. The ability to modify the chemistry and surface morphology of the coating by fine control of bath composition, pH, and temperature makes electrochemical deposition a versatile process for deposition of coatings on implants, with a tailored body response.

1. Introduction

Apatite is the primary inorganic constituent of all mammalian skeletal and dental tissues. It belongs to the family of calcium phosphates (CaP), which includes, among others, hydroxyapatite (HAp, $\text{Ca}_5(\text{PO}_4)_3(\text{OH})$), α - and β -tricalcium phosphates (TCP, $\text{Ca}_3(\text{PO}_4)_2$), octacalcium phosphate (OCP, $\text{Ca}_4(\text{HPO}_4)(\text{PO}_4)_2 \cdot 2.5\text{H}_2\text{O}$), dibasic calcium phosphate dihydrate (brushite, DCPD, $\text{CaHPO}_4 \cdot 2\text{H}_2\text{O}$), dibasic calcium phosphate anhydrous (monetite, DCPA, CaHPO_4), and amorphous calcium phosphate (ACP, $\text{Ca}_3(\text{PO}_4)_2 \cdot x\text{H}_2\text{O}$, $x = 3\text{--}4.5$). Biological apatites deviate from the stoichiometric composition of HAp, and contain small amounts of Mg^{2+} , Na^+ , K^+ , CO_3^{2-} , Cl^- and F^- . In their synthetic form, apatites are typically bioactive ceramics, which are more osteoconductive than metal surfaces, and form direct bonds with adjacent hard tissues. Hence, several types of synthetic apatites are now commercially available for use in bone repair, bone augmentation, bone substitution, and as coatings on dental and orthopedic implants.

Several methods have been explored to deposit CaP coatings in order to enhance implant fixation. Plasma spraying is the most common technology used commercially. Since the early 1990s, however, much interest in electrodeposition has evolved due to (1) the low temperatures involved, which enable formation of highly crystalline deposits with low solubility in body fluids and low residual stresses, (2) the ability to coat porous, geometrically complex, or non-line-of-sight surfaces, (3) the ability to control the thickness, composition, and microstructure of the deposit, (4) the possible improvement of the substrate/coating bond strength, and (5) the availability and low cost of equipment.

The performance of CaP coatings, both in vitro and in vivo, depends markedly on their chemical composition, crystallographic structure, surface morphology, surface roughness, and

porosity. Hacking et al., for instance, have shown that topography is more dominant than chemistry in providing HAp-coated implants with good osseointegration.¹ In addition, local changes in the chemistry and pH of body fluids may be responsible for the variation in the size and shape of bone apatite crystals. If so, the study of electrocrystallization in vitro may aid in better understanding the process of biomineralization and the factors that govern it in vivo. Thus, the objective of this work is to demonstrate the effects of the electrolyte solution composition, pH, and temperature on the microscopic and macroscopic characteristics of the resulting CaP deposits on CP-Ti.

2. Experimental Section

A sheet made of CP-Ti grade 2 (supplied by Scope Metal Trading and Technical Services Ltd.) was used as a cathode. Square specimens, $10 \times 10 \text{ mm}^2$, were cut from the 5-mm-thick sheet. Prior to electrodeposition, the exposed surfaces were mechanically ground on SiC papers from P120 to P1000 grit. Next, the electrodes were washed thoroughly with running deionized (DI) water, rinsed, ultrasonically degreased with acetone, and dried. Electrodeposition was carried out by means of a standard three-electrode cell, where platinum foil was used as the anode, and a saturated calomel electrode (SCE) was used as the reference electrode.

The electrolyte solution used for the electrodeposition of CaP was based on calcium nitrate ($\text{Ca}(\text{NO}_3)_2$) and ammonium dihydrogen phosphate ($\text{NH}_4\text{H}_2\text{PO}_4$), both AR-grade from Merck (Darmstadt, Germany). The powders were dissolved in Millipore water (Milli-DI). Two types of solutions were prepared: (i) 0.61 mM $\text{Ca}(\text{NO}_3)_2$, 0.36 mM $\text{NH}_4\text{H}_2\text{PO}_4$, $\text{pH}_0 = 6.0$; and (ii) 20 mM $\text{Ca}(\text{NO}_3)_2$, 12 mM $\text{NH}_4\text{H}_2\text{PO}_4$, $\text{pH}_0 = 4.2$. The bath composition and pH values were matched based on the solubility isotherm for HAp in the ternary system $\text{Ca}(\text{OH})_2\text{--H}_3\text{PO}_4\text{--H}_2\text{O}$.² The rationale behind choosing these two pH values was that on surgical insertion of a new implant, the pH of the body fluid in vicinity of the implant may drop to as low as 4.0, for example, due to bacterial infection. This condition may last for several weeks, thus affecting the biomineralization process. In addition, different electrocrystallization modes could be expected due to more than one order of magnitude difference between the concentrations of ions in the two solutions. In order to modify the ionic strength of the solution, 0.01, 0.1 or 1 M additive (either potassium chloride, KCl, or sodium nitrite, NaNO_2) was added to some baths. The pH was adjusted to its

* Corresponding author. Tel: +972-3-6407384. Fax: +972-3-6407617. E-mail: neliaz@eng.tau.ac.il.

† Present address: Department of Biomedical Engineering, SMK FOMRA Institute of Technology, Thaiyur Village, Kelambakkam 603103, India.

initial desired value by either HCl or NaOH additions, and measured by InoLab pH/Oxi Level 3 meter (WTW). During the electrodeposition process itself, CO₂-free nitrogen gas (99.999% purity) was continuously purged into the electrolyte to minimize the risk of contamination of the deposits by carbonates. In addition, stirring was carried out. A Lauda Ecoline E-220T thermostatic bath was used to maintain a constant temperature (within the range 60 to 95 ± 0.1 °C). An EG&G/PAR 263A potentiostat/galvanostat was employed to maintain the cathode potential at -1.4 V vs SCE for 2–3 h.

The samples were weighed before and after deposition, using an electronic balance (Sartorius' Basic BA 210 S). Mean weight values were calculated for five samples deposited under identical conditions. Phase identification was carried out by X-ray diffraction (XRD). To this aim, a Θ - Θ powder diffractometer from Scintag, equipped with a liquid nitrogen-cooled germanium solid-state detector and Cu K α radiation source, was used. The data was collected at a scan rate of 1°/min, from 2 Θ = 20° to 60°. Fourier transform infrared spectroscopy (FT-IR) was used to determine the vibration modes characteristic of the CaP coating. For this purpose, a Vector 200 spectrometer from Bruker, operated in the attenuated total reflectance (ATR) mode, was used. The morphology of the deposits after drying was imaged by scanning electron microscope (SEM, Jeol model JSM-6300). The attached energy dispersive spectroscopy (EDS, Oxford Isis system) was used to estimate the Ca/P ratio as well as to identify other elements present in the deposit. A PicoSPM (Molecular Imaging) electrochemical atomic force microscope (EC-AFM) was used *ex situ*. Imaging was done under contact mode, using tips made of Si₃N₄ (Veeco). Both topography and deflection (error signal) images were acquired, the latter representing the gradient of shape change. The mean length and mean width of the CaP crystals were determined by direct measurement of features on the deflection image. The mean thickness, on the other hand, was determined from line scans on the topography image. Metallographic cross-sections were also prepared and analyzed. The morphology and thickness of the coating were evaluated from the cross-sections by means of Olympus IX71 light microscope, equipped with ColorView II CCD camera and analySISdocu software package, both from Soft Imaging System. The thickness of the coating was also measured by SEM.

Corrosion measurements of both uncoated and coated samples were carried out in Ringer's simulated body fluid (SBF, 8.60 g L⁻¹ NaCl, 0.33 g L⁻¹ CaCl₂, 0.30 g L⁻¹ KCl) at pH = 7.4 and *T* = 37 ± 0.1 °C. For the corrosion tests, an EG&G/PAR 263A potentiostat/galvanostat and a CorrWare/CorrView (ver. 2.6b) software package from Scribner Associates, for data acquisition and data analysis, were used. First, the open-circuit potential (OCP) was monitored as a function of time for 60 min, or until a stable potential (namely, the corrosion potential, *E*_{corr}) was attained. Next, a cyclic potentiodynamic polarization measurement was carried out. The potential was scanned from -0.25 V vs OCP to +4.5 V vs SCE at a sweep rate of 10 mV min⁻¹; then, the scan was reversed in the negative direction.

3. Results and Discussion

Typical current density transients, monitored during potentiostatic deposition of CaP at 90 °C, are shown in Figure 1a,b for baths at pH₀ = 6.0 and pH₀ = 4.2, respectively. The shape of the transients in Figure 1a is typical of electrodeposition in the presence of overlap between diffusion fields around growing nuclei. This shape has been associated with precipitation of HAP from solution, following two stages: (1) instantaneous nucleation, two-dimensional growth; (2) progressive nucleation, three-dimensional growth.³ The shape of the current transients in Figure 1b is much different. The current density value at steady state is similar to that at the maximum in Figure 1a, although it typically takes less time to reach the latter. On the other hand, it takes longer times to reach steady state in Figure 1a, and the current density value at steady state is less than half that in Figure 1b. This difference could, in principle, be related to the higher concentrations of ions in the solution at pH₀ = 4.2, which increase the driving force for diffusion-related phenomena. It is well-known that changes in the surface state of the substrate, in the overpotential, and in the solution concentration close to

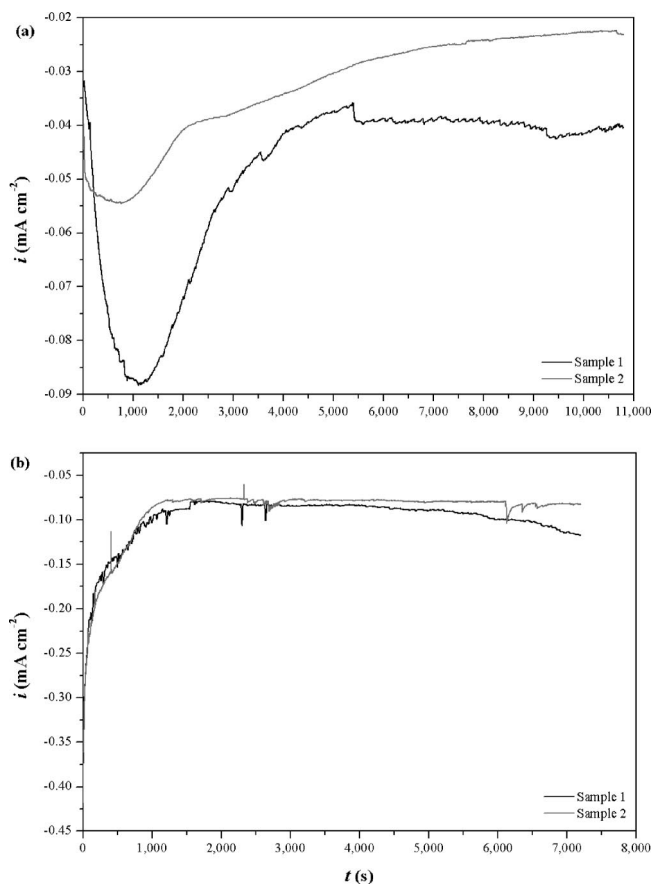


Figure 1. Current density transients during potentiostatic deposition of CaP on CP-Ti at 90 °C: (a) pH₀ = 6.0, (b) pH₀ = 4.2.

the surface may all affect the shape of the current transient significantly. Different current transients may represent different electrochemical processes that take place. As will be shown below, the difference in the shape of the current transients represents also a difference in the nature of the deposit formed; coatings deposited at pH₀ = 4.2 were thicker and exhibited different surface morphology, chemistry, and phase composition.

The phases present in different coatings were identified by means of XRD. Indexing was made with reference to the JCPDS files for pure Ti (#44-1294), HAP (#09-0432), OCP (#44-0778 and 26-1056), α -TCP (#09-0348), β -TCP (#09-0169), brushite (#09-0077 and 11-0293), and monetite (#09-0080, 04-0513 and 03-0398). When comparing the measured *d* values to those in the standard files, it was not always possible to index the reflections based on a deviation smaller than ±0.01 Å. The shift in the measured reflections may be associated with the non-powder character of the electrodeposited samples, different processing techniques, distortions in the unit cell dimensions, etc. Figure 2a compares typical XRD spectra for coatings deposited for 3 h from a bath at pH₀ = 4.2, at different temperatures. In all patterns, reflections (002), (101), (102) and (100) from the titanium substrate are evident, indicating that the coating is either very thin or porous. When comparing to JCPDS file #44-1294, it becomes apparent that these reflections represent a nonrandom, preferred orientation (texture) of the substrate, with its grains being oriented with their {002} planes parallel to the sheet surface. This may be attributed, for example, to well-defined, platy habits in titanium.⁴ At all temperatures, HAP is the primary constituent of the coating. Its strongest reflection at ~26° indicates that it has a preferred orientation along the {002} planes. The high frequency of these planes may

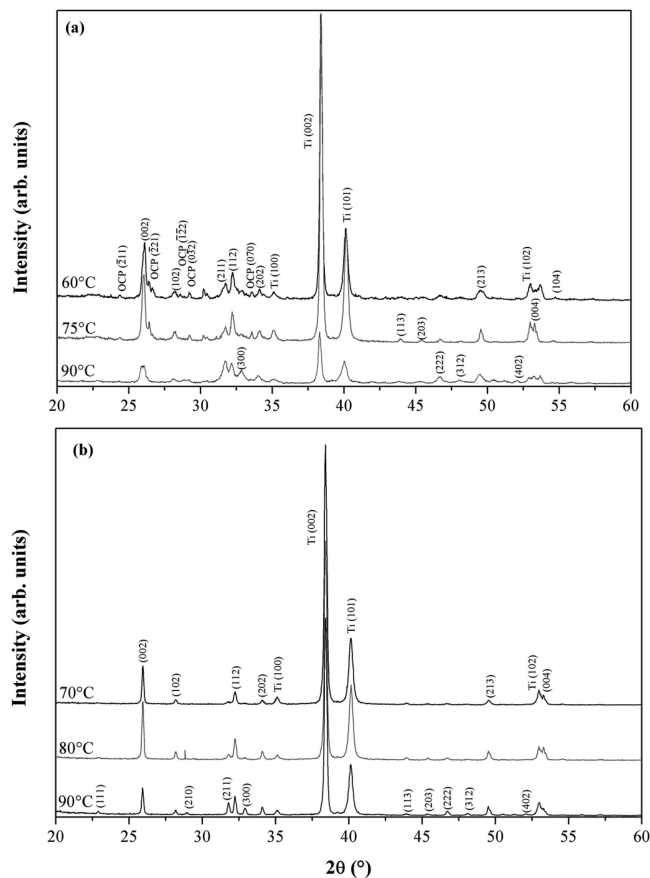


Figure 2. The effect of bath temperature on the XRD spectra from coatings deposited for 3 h from a bath at (a) $\text{pH}_0 = 4.2$ and (b) $\text{pH}_0 = 6.0$.

be related to a plate-like morphology, as evident in Figure 8a–d. As a result of a strong preferred orientation, the peak intensities cannot be related to those expected from the powder diffraction file.⁴ This texture becomes less pronounced at 90 °C. A similar phenomenon of preferred orientation of apatite coatings on titanium substrates has been reported before.^{3,5,6} In some coatings deposited from the bath at $\text{pH}_0 = 4.2$, OCP was found to coexist along with HAP. Its characteristic reflections are marked by “OCP” in Figure 2a. The possible presence of traces of DCPA was found ambiguous. As a result of increasing the bath temperature to 90 °C, the presence of OCP was eliminated. It has been observed that pH values lower than 4.4 require higher temperatures for precipitation of HAP.⁷

Figure 2b compares typical XRD spectra for coatings deposited at different temperatures for 3 h from a bath at $\text{pH}_0 = 6.0$. In this case, all reflections are assigned to HAP and to the base metal, but not to any other CaP phase. Preferred orientation of both the substrate and the HAP coating is also evident. The peaks in Figure 2b are sharper and narrower than those in Figure 2a. This observation indicates that the level of crystallinity in the coatings deposited from the bath at $\text{pH}_0 = 6.0$ is higher than that in coatings deposited from the bath at $\text{pH}_0 = 4.2$. Previously, the content of the noncrystalline phase in a coating deposited at 85 °C from a bath at $\text{pH}_0 = 6.0$ was measured as less than 5%.⁸ It is well-known that stoichiometric HAP coatings are more crystalline, and therefore less soluble in vitro and in vivo, than other CaP coatings. This could be of benefit in increasing the long-term durability of such coatings when applied on orthopedic implants. Dividing the intensity of the (002) reflection of HAP by the (002) reflection of the Ti

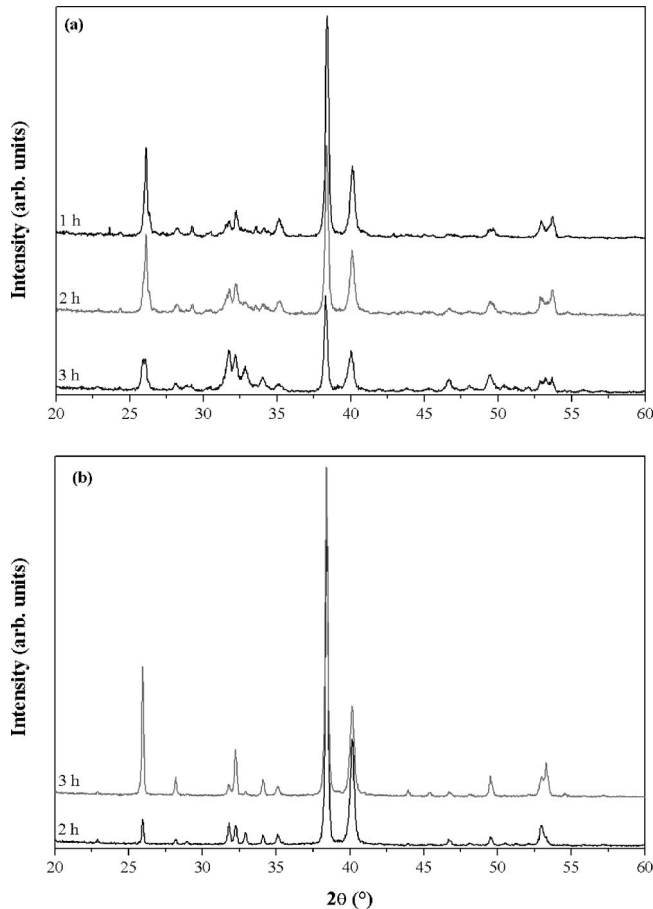


Figure 3. The effect of deposition time on the XRD patterns from samples coated at (a) $\text{pH}_0 = 4.2$, $T = 90$ °C; and (b) $\text{pH}_0 = 6.0$, $T = 85$ °C.

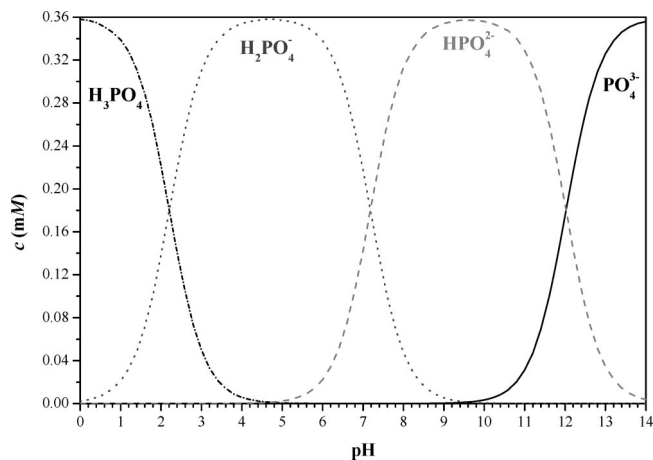


Figure 4. The distribution of phosphate species as a function of pH at 37 °C, 0.36 mM total analytical concentration of phosphate, and free hydrogen concentration of 10^{-6} M.

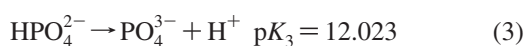
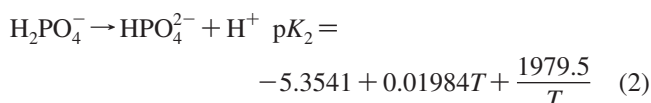
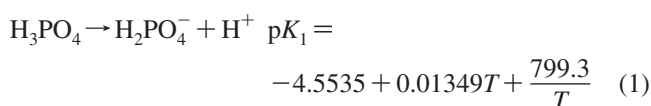
substrate, for the same bath temperature, results in higher values for the bath at $\text{pH}_0 = 4.2$. This implies that the coatings deposited at $\text{pH}_0 = 4.2$ are thicker than those deposited at $\text{pH}_0 = 6.0$, or that the latter are more porous.

Figure 3 demonstrates the effect of deposition time on the XRD patterns. Figure 3a represents deposition at 90 °C from a bath at $\text{pH}_0 = 4.2$, whereas Figure 3b represents deposition at 85 °C from a bath at $\text{pH}_0 = 6.0$. As expected, the ratio between the strongest reflection of the coating and the strongest reflection

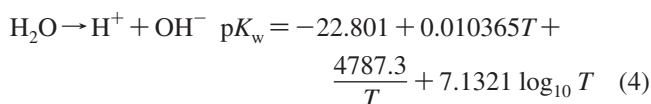
of the substrate increases (for each bath) with deposition time, thus indicating an increase in coating thickness. Already after 1 h, no evidence exists for precursor phases, such as OCP that was previously identified.⁹ At $\text{pH}_0 = 4.2$, the intensities of the (211) and (112) reflections of HAp become more prominent in comparison to its (002) reflection as the deposition time is increased from 1 to 3 h.

The electrolyte solutions in this study contained dihydrogen phosphate. Its deprotonation reaction, forming HPO_4^{2-} , serves as an important biological buffer system, which operates in the internal fluid of all cells, stabilizing the pH at around 7.21 (in mammals, $\text{pH} = 6.9\text{--}7.4$). Thus, the speciation curves of phosphoric acid may aid, at least to some extent, in understanding the effect of pH on the electrocrystallization of CaP. In this work, the chemical equilibrium code ChemEQL version 3.0¹⁰ was used to generate the speciation curves shown in Figure 4.

Equations 1 through 3, which define the temperature dependence of the dissociation constants of phosphoric acid,¹¹ allowed for making speciation calculations at different solution temperatures:



At 37 °C one gets $\text{p}K_1 = 2.207$, $\text{p}K_2 = 7.182$, and $\text{p}K_3 = 12.023$. Similar values have been reported elsewhere.^{12,13} The ionic product of water was calculated from¹⁴



Thus, at 37 °C one gets $\text{p}K_w = 13.62$.

Figure 4 shows the speciation of phosphoric acid at 37 °C. The total analytical concentration of phosphate was defined as 0.36 mM, and the free concentration of the hydrogen cation was defined as 10^{-6} M. The decrease in the density of water as the bath temperature is increased to 37 °C was neglected. This figure shows that once the solution was prepared, some of the H_2PO_4^- ions deprotonated, forming HPO_4^{2-} . For pH values in the range of 7.2–12.0, the predominant species is HPO_4^{2-} , whereas above $\text{pH} = 12.0$ the triply charged anion PO_4^{3-} becomes the most abundant species. Similar calculations can be made for the bath at $\text{pH}_0 = 4.2$. In this case, however, some of the H_2PO_4^- ions immediately protonate, forming H_3PO_4 . It should be emphasized that only orthophosphate salts are considered herein, because metaphosphates and pyrophosphates hydrolyze in body fluids. It should also be noted that, based on calculations of the limiting current density for all possible cathodic reactions, Eliaz and Eliyahu concluded that, in a bath initially at $\text{pH} = 6.0$, H_2PO_4^- is indeed the primary supplier of PO_4^{3-} ions, which are necessary for the precipitation of HAp.³ It was also explained that the local pH in vicinity of the working electrode surface must first increase before significant precipitation of HAp could take place. This was recently supported by the observation of incubation period in real-time electrochemical quartz crystal microbalance (EQCM) measurements.⁹

In order to validate Figure 4, the calculation was repeated, using PHREEQC version 2 geochemical computer program.¹⁶

This powerful program for Windows was written in the C-language. Although the program is based on equilibrium chemistry of aqueous solutions interacting with minerals, gases, solid solutions, exchangers and sorption surfaces, it also includes the capability to model kinetic reactions. Thus, it has gained much popularity in simulating chemical reactions and transport processes in natural or polluted waters. This program has already been applied in studies of CaP precipitation.^{17–21} While PHREEQC is more powerful than ChemEQL, it is also more complicated to operate and requires additional input, for example, $\text{p}E$ (a measure of the availability of electrons in the solution and, thus, of the solution's reducing power). Therefore, it was decided to compare the output of both programs for the simplest case of solution chemistry, that is, the one that contains only species of phosphoric acid. When defining in the input file $\text{p}E = 4$ and alkalinity = 2.0 for the phosphate master species (used in the mole-balance equation for alkalinity), PHREEQC gave exactly the same results as ChemEQL.

The next step is to determine the synergistic effects of bath temperature, pH, and composition on the ionic strength, free ion activities product (IAP) and saturation index (SI) of various CaP phases. To this aim, PHREEQC was used. The activities were calculated using the Debye–Hückel equation for very dilute solutions:

$$\log_{10} \gamma_{\pm} = -A z_i^2 \sqrt{I} \quad (5)$$

where γ_{\pm} is the mean ionic activity coefficient, A is a temperature-dependent constant, z_i is the ionic charge of the aqueous species i , and I is the ionic strength of the solution, defined as

$$I = \frac{1}{2} \sum_{i=1}^n c_i z_i^2 \quad (6)$$

where c_i is the analytical concentration of species i . The constant A is calculated as

$$A = 1.8246 \times 10^6 (\epsilon_w T)^{-3/2} [\text{dm}^3 \cdot \text{mol}^{-1}]^{1/2} \quad (7)$$

where ϵ_w is the dielectric constant of water and T is the absolute temperature (in Kelvin degrees). It is recognized here that the dielectric constant of dilute solutions is the same as the dielectric constant of water. Its temperature dependence was taken into account using the fitting equation:¹⁵

$$\epsilon_w = 88.089514 - 0.405316T + 8.832192 \times 10^{-4} T^2 - 9.737740 \times 10^{-7} T^3 \quad (8)$$

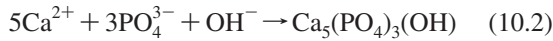
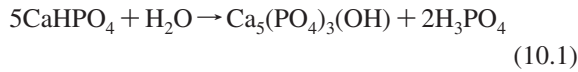
in which T is substituted in Celsius degrees. Substituting $T = 25$ °C into this equation, one gets the well-known value $\epsilon_w = 78.5$.

The SI of a solution with respect to a precipitate phase is defined as

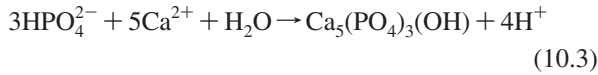
$$SI = \log_{10} \left(\frac{\text{IAP}}{K_{\text{sp}}} \right) \quad (9)$$

where K_{sp} is the thermodynamic solubility product. When $SI = 0$, the solution is in equilibrium (mineral reacts fast enough to maintain equilibrium). On the other hand, $SI < 0$ and $SI > 0$ indicate undersaturation (mineral should dissolve) and supersaturation (mineral should precipitate spontaneously), respectively. At low positive values of SI , a metastable zone may also exist. In this zone, although the solution is already supersaturated, the kinetics of precipitation is very slow.¹⁷

Several chemical reactions may all result in the formation of HAp, for example¹⁹



and



The ion activities products for different CaP phases are defined as

$$\text{IAP}(\text{HAp}) = a_{\text{Ca}^{2+}}^5 a_{\text{PO}_4^{3-}}^3 a_{\text{OH}^-} \quad (11.1)$$

$$\text{IAP}(\text{DCPD}) = a_{\text{Ca}^{2+}} a_{\text{HPO}_4^{2-}} \quad (11.2)$$

$$\text{IAP}(\text{OCP}) = a_{\text{Ca}^{2+}}^4 a_{\text{PO}_4^{3-}}^3 a_{\text{H}^+} \quad (11.3)$$

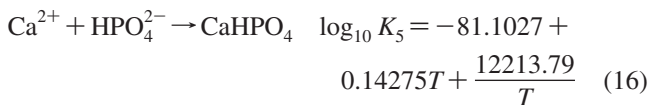
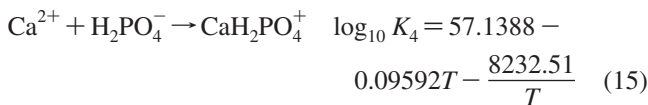
etc. The temperature dependence of the solubility product of several calcium phosphates may be defined as^{21,22}

$$\log_{10} K_{\text{sp}}(\text{HAp}) = -1.6657 - 0.098215T - \frac{8219.41}{T} \quad (12)$$

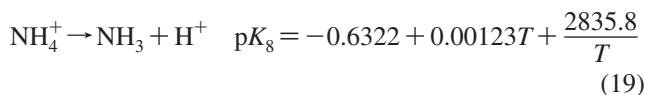
$$\log_{10} K_{\text{sp}}(\text{DCPD}) = 18.180752 - 0.0420307T - \frac{3649.5701}{T} \quad (13)$$

$$\log_{10} K_{\text{sp}}(\text{DCPA}) = 8.4463 - 0.03156T - \frac{1774.7676}{T} \quad (14)$$

At 25 °C, for example, eq 12 predicts $\text{p}K_{\text{sp}}(\text{HAp}) = 58.51$, a well-known value.¹⁷ In addition to these equations, the $\text{p}K_{\text{sp}}$ value for OCP at 37 °C equals 48.7.²³ In the precipitation calculations, data on several ion pairs is also needed, including²³



For nitrogen species:¹⁴



Finally, the temperature dependence of the density of water within the temperature range 0–100 °C may be described by the equation:¹⁵

$$\begin{aligned} \text{sign}[T(^{\circ}\text{C}) - 4] \times (1 - \rho_w)^{0.49} = \\ 3859.614322 \left[\frac{1}{T(^{\circ}\text{K})} - \frac{1}{273.15} \right]^2 - \\ 220.434893 \left[\frac{1}{T(^{\circ}\text{K})} - \frac{1}{273.15} \right] - 0.011067 \quad (20) \end{aligned}$$

where ρ_w is the density of water at a given temperature T , in units of g cm^{-3} .

PHREEQC was used to evaluate the possible precipitation in each of the two solutions (0.61 mM $\text{Ca}(\text{NO}_3)_2$, 0.36 mM $\text{NH}_4\text{H}_2\text{PO}_4$, free hydrogen concentration 1.0×10^{-6} M; 20 mM $\text{Ca}(\text{NO}_3)_2$, 12 mM $\text{NH}_4\text{H}_2\text{PO}_4$, free hydrogen concentration 6.3×10^{-5} M), at either $T = 60$ °C or $T = 90$ °C (the two extreme temperatures).

At $T = 60$ °C: $\text{p}K_1 = 2.339$, $\text{p}K_2 = 7.197$, $\text{p}K_3 = 12.023$, $\text{p}K_4 = -0.475$, $\text{p}K_5 = -3.111$, $\text{p}K_6 = -6.462$, $\text{p}K_7 = -1.301$, $\text{p}K_8 = 8.293$, $\text{p}K_w = 13.017$, $\varepsilon_w = 66.74$, $A = 0.551$ ($\text{dm}^3 \cdot \text{mol}^{-1}$)^{1/2}, $\rho_w = 0.983$ $\text{g} \cdot \text{cm}^{-3}$, $\text{p}K_{\text{sp}}(\text{HAp}) = 59.054$, $\text{p}K_{\text{sp}}(\text{DCPD}) = 6.775$, $\text{p}K_{\text{sp}}(\text{DCPA}) = 7.393$, and $\text{p}K_{\text{sp}}(\text{OCP}) \sim 48.7$.

At $T = 90$ °C: $\text{p}K_1 = 2.545$, $\text{p}K_2 = 7.301$, $\text{p}K_3 = 12.023$, $\text{p}K_4 = +0.359$, $\text{p}K_5 = -4.362$, $\text{p}K_6 = -6.462$, $\text{p}K_7 = -1.301$, $\text{p}K_8 = 7.626$, $\text{p}K_w = 12.407$, $\varepsilon_w = 58.06$, $A = 0.596$ ($\text{dm}^3 \cdot \text{mol}^{-1}$)^{1/2}, $\rho_w = 0.966$ $\text{g} \cdot \text{cm}^{-3}$, $\text{p}K_{\text{sp}}(\text{HAp}) = 59.961$, $\text{p}K_{\text{sp}}(\text{DCPD}) = 7.130$, $\text{p}K_{\text{sp}}(\text{DCPA}) = 7.899$, and $\text{p}K_{\text{sp}}(\text{OCP}) \sim 48.7$.

Figure 5 shows the pH dependence of the ionic strength of the solution (line) and the saturation indices of HAp, OCP, DCPA and DCPD (lines with symbols). In Figure 5a,c the solution was that with initial $\text{pH}_0 = 4.2$, whereas Figure 5b,d represents the solution initially at $\text{pH}_0 = 6.0$. While Figure 5a,b represents baths at $T = 60$ °C, Figure 5c,d represents baths at $T = 90$ °C. Thus, the synergistic effects of bath composition, pH and temperature can be deduced. In Figure 5a, the ionic strength first decreases a little bit and then increases as the pH is increased. The increase in the ionic strength is divided into two stages: slow over a wide pH range, and rapid at high pH values. According to this figure, both DCPA and DCPD have $\text{SI} < 0$ over the whole pH range and are therefore not expected to be present in the deposit. The presence of HAp in the deposit requires from a thermodynamic standpoint that a pH of at least 7.2 is first established in vicinity to the surface of the cathode. OCP is expected to precipitate spontaneously over the whole pH range. The solution is always more supersaturated with respect to OCP than with respect to HAp. As the pH is increased, the level of saturation of HAp is increased (up to $\text{pH} = 11.6$), while those of DCPA, DCPD and OCP are decreased. Comparison to Figure 5b allows to determine the effect of bath composition at $T = 60$ °C. As a result of decreasing the analytical concentrations of $\text{Ca}(\text{NO}_3)_2$ and $\text{NH}_4\text{H}_2\text{PO}_4$ in the initial solution, the ionic strength of the solution is decreased in Figure 5b. However, HAp becomes significantly supersaturated over the whole pH range. OCP may exist in the deposit only if the pH reached 7.4–11.8 during the process. DCPA may form within the range $\text{pH} = 7.6$ –8.6, although its level of supersaturation is very low. DCPD is not expected to be present in the deposit. In order to understand the origin of the increase of the SI of HAp when the pH is raised from 4.2 to 7.2 in Figure 5a, the activities (in molal units) of the different species in solution are compared in Table 1. It is evident that only the increase in the activity of the hydroxyl anion makes the IAP high enough to allow spontaneous precipitation of HAp. The activities of different ion pairs are also comparable, as listed in Table 1. The increase in the SI of HAp when the pH is increased

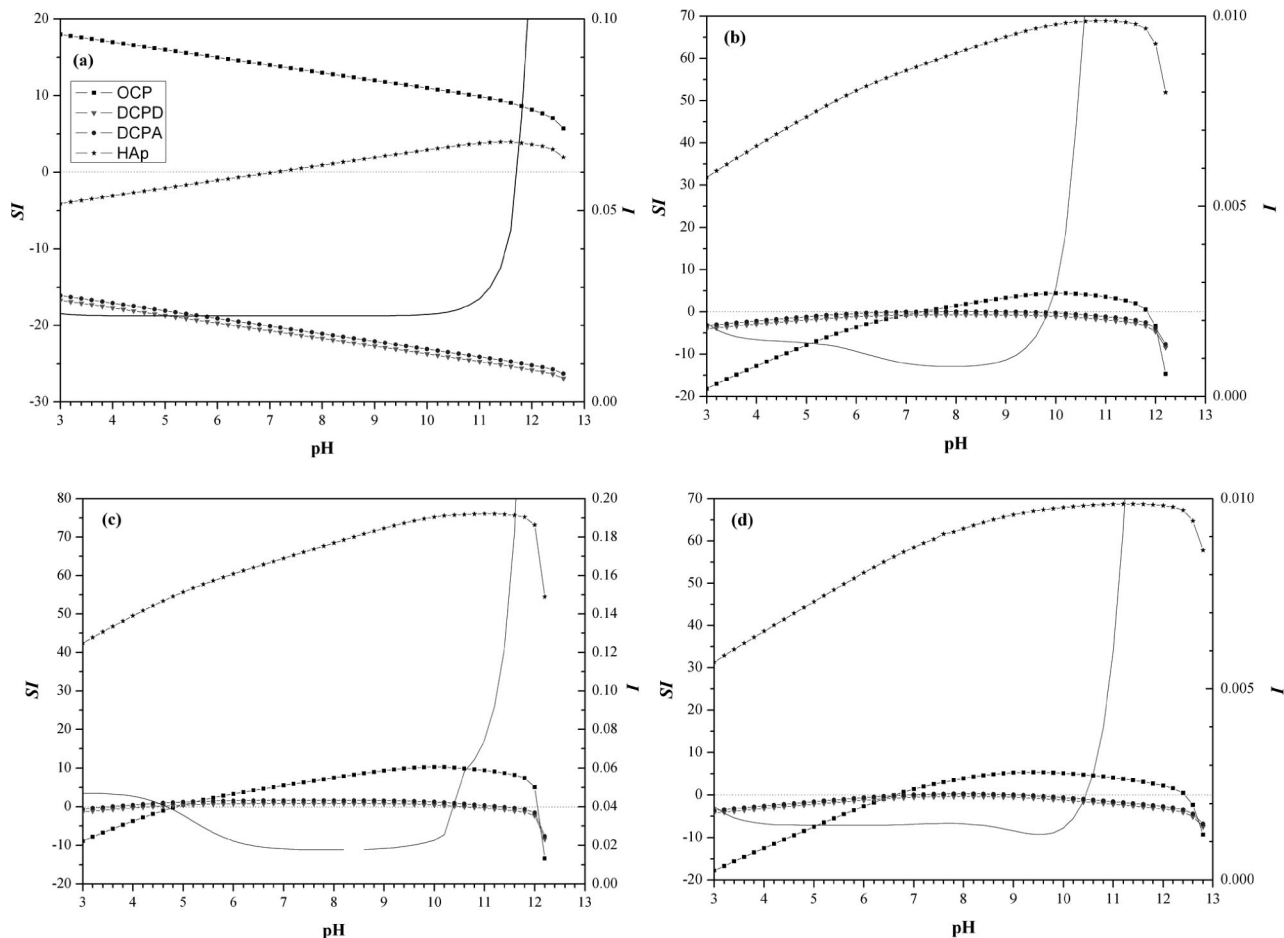


Figure 5. The dependence of the ionic strength (I) and the saturation indices (SI) of four different calcium phosphates on the analytical composition of the solution as well as on its pH and temperature. The I values are drawn as a solid line, whereas the SI values are drawn as lines with symbols. (a) Solution ii, $T = 60$ °C, (b) Solution i, $T = 60$ °C, (c) Solution ii, $T = 90$ °C, and (d) Solution i, $T = 90$ °C.

Table 1. The Activities (in Molal Units) of Species in Different Solutions

solution ^a	T (°C)	pH	Ca^{2+}	PO_4^{3-}	OH^-	HPO_4^{2-}	CaHPO_4	CaPO_4^-	CaOH^+	$\text{CaH}_2\text{PO}_4^+$
ii	60	4.2	4.50×10^{-3}	7.76×10^{-7}	1.52×10^{-9}	4.64×10^{-23}	2.70×10^{-22}	1.01×10^{-2}	1.37×10^{-10}	2.50×10^{-36}
ii	60	7.2	4.51×10^{-3}	7.76×10^{-7}	1.52×10^{-6}	4.64×10^{-26}	2.70×10^{-25}	1.01×10^{-2}	1.37×10^{-7}	0
i	60	7.2	4.53×10^{-4}	1.92×10^{-9}	1.52×10^{-6}	1.28×10^{-4}	7.49×10^{-5}	2.53×10^{-6}	1.38×10^{-8}	1.72×10^{-7}
ii	90	7.2	4.85×10^{-3}	1.62×10^{-9}	6.20×10^{-6}	1.08×10^{-4}	1.20×10^{-2}	2.28×10^{-5}	6.02×10^{-7}	2.89×10^{-7}
i	90	7.2	3.07×10^{-4}	5.87×10^{-10}	6.21×10^{-6}	3.90×10^{-5}	2.75×10^{-4}	5.21×10^{-7}	3.81×10^{-8}	6.61×10^{-9}

^a (i) 0.61 mM $\text{Ca}(\text{NO}_3)_2$, 0.36 mM $\text{NH}_4\text{H}_2\text{PO}_4$, $\text{pH}_0 = 6.0$. (ii) 20 mM $\text{Ca}(\text{NO}_3)_2$, 12 mM $\text{NH}_4\text{H}_2\text{PO}_4$, $\text{pH}_0 = 4.2$.

from 4.2 to 7.2 cannot be associated with increase in the activities of species such as CaHPO_4 or HPO_4^{2-} (see eqs 10.1 and 10.3, respectively). Comparison is made between the species distribution at $\text{pH} = 7.2$ in solutions with different compositions at 60 °C (Figure 5a,b). The higher SI in Figure 5b cannot be explained in terms of increase in the activities of the calcium cations, phosphate and hydroxyl anions. Instead, CaHPO_4 or HPO_4^{2-} may have become more dominant in the formation of HAp.

Comparison between Figure 5c and Figure 5a allows for determining the effect of bath temperature. As a result of increasing the temperature, the ion strength did not change significantly, albeit a less steady behavior is observed at 90 °C. However, the solution at 90 °C becomes most supersaturated with respect to HAp no matter the pH is, and its SI value is higher and positive throughout the whole pH range. The SI value for OCP is positive only within the range $\text{pH} = 5.0$ through 12.0. There is also pH range within which both DCPA and DCPD may precipitate. The distribution of species at $T = 90$

°C is listed in Table 1. The increased $SI(\text{HAp})$ value at the higher temperature may be attributed primarily to the significant increase in the activities of CaHPO_4 and HPO_4^{2-} .

Finally, comparison of Figure 5d to Figure 5c allows determining the effect of solution composition while its comparison to Figure 5b allows determining the effect of temperature. The ionic strength of the solution in Figure 5d is slightly lower than that of the other two solutions. In Figure 5d, only the SI of HAp is positive throughout the whole pH range. Its value is similar to that in Figure 5b, that is, the temperature difference is not significant with respect to the stability of the HAp phase. At 90 °C, OCP may also be stable at pH values between 6.8 and 12.4, while a very low level of supersaturation of DCPA exists between $\text{pH} = 7.0$ and $\text{pH} = 9.0$. The distribution of species at $T = 90$ °C and $\text{pH} = 7.2$ is listed in Table 1. The species distribution in the solution containing analytical concentrations of 0.61 mM $\text{Ca}(\text{NO}_3)_2$ and 0.36 mM $\text{NH}_4\text{H}_2\text{PO}_4$ does not change significantly when the solution temperature is raised from 60 to 90 °C. However,

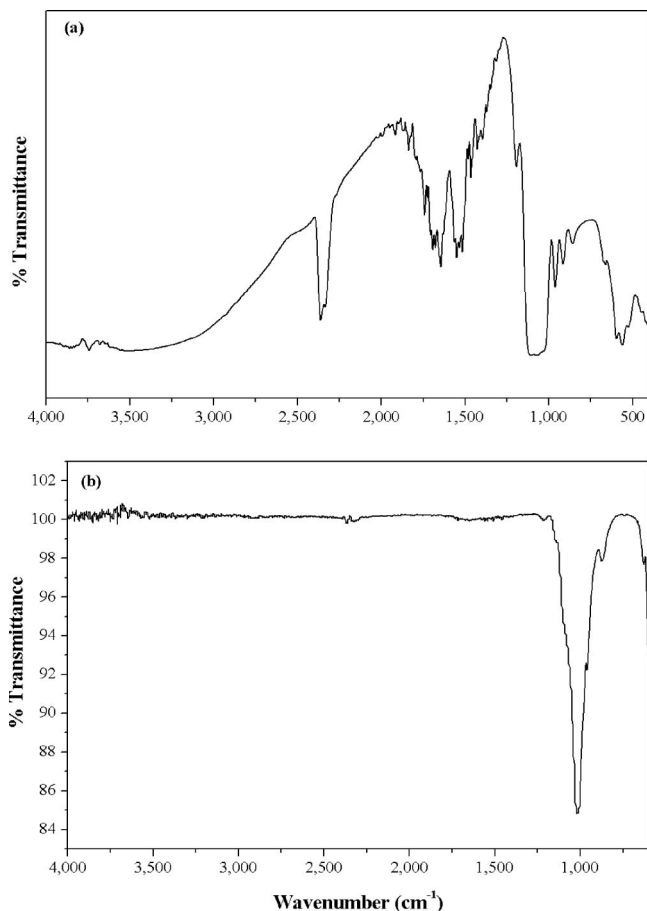


Figure 7. FT-IR spectra from Ti samples coated with CaP at: (a) $\text{pH}_0 = 4.2$, $T = 90\text{ }^\circ\text{C}$, $t = 2\text{ h}$; and (b) $\text{pH}_0 = 6.0$, $T = 85\text{ }^\circ\text{C}$, $t = 2\text{ h}$.

stretching vibration because of the stoichiometry of HAp. A band in the region $\sim 950\text{--}980\text{ cm}^{-1}$ results from the ν_1 stretching vibration of PO_4^{3-} (see peak at 958 cm^{-1} in Figure 7b, and peak at 963 cm^{-1} in Figure 7a). The ν_3 band of PO_4^{3-} has mostly been indexed in the range $1040\text{--}1125\text{ cm}^{-1}$. Bands (ν_3) at $1370\text{--}1650\text{ cm}^{-1}$ are attributed to the presence of adsorbed (surface) CO_3^{2-} . The number of these peaks is higher in Figure 7a than in Figure 7b. The origin of this carbonate could be the atmosphere (e.g., in the IR chamber). The peaks around 2350 cm^{-1} are indicative of adsorbed CO_3^{2-} . Although these peaks are more distinct in Figure 7a than in Figure 7b, it should be noted that in other experiments distinct carbonate peaks were either observed also in coatings deposited at $\text{pH}_0 = 6.0$, or were much shallower in coatings deposited at $\text{pH}_0 = 4.2$. Thus, it cannot be concluded that carbonate contamination is more significant in baths at $\text{pH}_0 = 4.2$ than in baths at $\text{pH}_0 = 6.0$. It is well-known that the carbonate ion may substitute for either the hydroxyl or the phosphate ions in HAp. The $\text{CO}_3\text{-for-PO}_4$ substitution was shown to cause reduction in crystallinity and change in the shape of crystals from acicular to rod-shape, and then to equiaxed flat crystals.²⁸ However, in the present study CO_2 -free nitrogen gas was continuously purged into the electrolyte during the electrodeposition process, in order to eliminate the risk of contamination of the deposits by carbonates. Furthermore, a pH of 4.2 should be too acidic for the carbonate ion to be stable in solution. In fact, no reflections of carbonate-containing CaP phases were observed in the XRD patterns. Hence, it may be concluded that the FT-IR bands of CO_3^{2-} may solely be attributed to carbonate contamination from air. A broadband in the range $2800\text{--}3600\text{ cm}^{-1}$ is attributed to

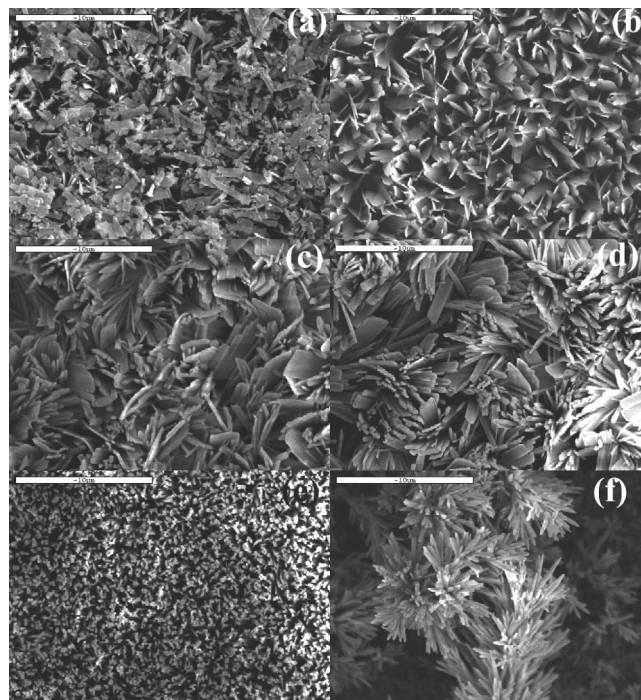


Figure 8. Typical surface morphologies (SEM images) of CaP coatings deposited under different conditions: (a) $\text{pH}_0 = 4.2$, $60\text{ }^\circ\text{C}$, 2 h ; (b) $\text{pH}_0 = 4.2$, $85\text{ }^\circ\text{C}$, 4 h ; (c) $\text{pH}_0 = 6.0$, $80\text{ }^\circ\text{C}$, 3 h ; (d) $\text{pH}_0 = 6.0$, $90\text{ }^\circ\text{C}$, 3 h ; (e) $\text{pH}_0 = 6.0$, $90\text{ }^\circ\text{C}$, 3 h , addition of 0.01 M KCl ; and (f) $\text{pH}_0 = 6.0$, $90\text{ }^\circ\text{C}$, 3 h , addition of 1.00 M NaNO_2 . All scale bars are $10\text{ }\mu\text{m}$.

the stretching vibrations of hydrogen-bonded adsorbed water and hydroxyl ions. Structural OH^- stretching peak at $\sim 3572\text{ cm}^{-1}$ is typical of HAp (and does not appear, for example, in the FT-IR spectrum of OCP). On the other hand, an extended noise at $\sim 3600\text{--}3900\text{ cm}^{-1}$ (see Figure 7) may indicate on a rather wet (i.e., not just hydrated) sample.

The spectrum from a coating deposited at $\text{pH}_0 = 4.2$ contains more peaks than the spectrum from a coating deposited at $\text{pH}_0 = 6.0$, although differences as those reported by Shirkanzadeh²⁹ are not evident. Yet, a small absorption peak at $\sim 525\text{ cm}^{-1}$ does appear in Figure 7a only. This peak may be assigned to the bending mode of the HPO_4^{2-} group, which is characteristic of crystalline acid phosphate, thus indicating the presence of OCP. The bands at 858 and 915 cm^{-1} may be attributed to the P-(OH) stretching mode of the acid orthophosphates groups. Bands in this region are characteristic of OCP and are useful in identifying its presence in mixtures with HAp. The peak at $\sim 1192\text{ cm}^{-1}$ is also believed to arise from hydrogen-bonded OH between $\text{O}_3\text{PO-H-OPO}_3$ groups of HPO_4^{2-} ions. The band at $\sim 2362\text{ cm}^{-1}$ is characteristic of calcium-deficient apatite, and corresponds to an interphosphate oxygen bond. The presence of OCP only in the coating deposited at $\text{pH}_0 = 4.2$ may mean that OCP is formed within a lower pH range compared to HAp, and serves as precursor to the formation of HAp.⁹

The typical surface morphology of different coatings is evident from the SEM images in Figure 8. Figure 8a shows one region observed within a coating deposited at $\text{pH}_0 = 4.2$ and $60\text{ }^\circ\text{C}$ for 2 h . The plate-like crystals are similar to those related to DCPA, DCPD and OCP under different solution conditions.^{27,29–33} The mean Ca/P atomic ratio (EDS) in this area was 1.35, much smaller than that of HAp, but close to that of OCP (1.33). Figure 8b shows the typical morphology of a CaP coating deposited at $\text{pH}_0 = 4.2$ and $85\text{ }^\circ\text{C}$ for 4 h . The

platelets morphology in this case is much different from that in Figure 8a. The Ca/P ratio was also significantly higher (1.65). This supports the finding in Figure 2a that, as the bath temperature was raised toward 90 °C, the OCP content decreased and the coating became richer in HAp. Figure 8c shows the typical morphology of a CaP coating deposited at $\text{pH}_0 = 6.0$ and 80 °C for 3 h. The platelets morphology in this case is similar to that in Figure 8b. The Ca/P ratio for the coating shown in Figure 8c was also 1.65. Note that each platelet seems to be composed of whiskers. Figure 8d shows the typical morphology of a CaP coating deposited at $\text{pH}_0 = 6.0$ and 90 °C for 3 h. This coating was found to be thicker than that in Figure 8c, in accordance with our previous observation of the effect of temperature,³⁴ and had $\text{Ca/P} = 1.63$.

Figure 8e shows the typical morphology of a CaP coating deposited in the presence of 0.01 M KCl at $\text{pH}_0 = 6.0$ and 90 °C for 3 h. Based on Figure 6a it has already been concluded that the addition of KCl to the plating bath resulted in thicker HAp coatings. From Figure 8e it is evident that the surface morphology was changed significantly too, to needles (likely, hexagons) that protrude upward from the substrate. The coating is relatively dense and uniformly distributed, with only small pores. On the basis of EDS analysis, the mean Ca/P ratio in this coating equaled 1.63. It should be noted that when the concentration of KCl in the bath was increased to 0.10 M and then to 1.00 M, the Ca/P ratio in the coating was increased to 1.70 and 2.13, respectively. Thus, the presence of KCl seems to result in Ca-enriched deposits. In addition, when the concentration of KCl in the bath was 1.00 M, the CaP coating became nonuniform and contained large pores. Figure 8f shows the typical morphology of a CaP coating deposited in the presence of 1.00 M NaNO_2 at $\text{pH}_0 = 6.0$ and 90 °C for 3 h. The dendritic morphology is clearly different from the other surface morphologies described above. A similar dendritic morphology was also observed when the concentration of NaNO_2 in the bath was reduced to 0.10 and 0.01 M. The Ca/P ratio in all three cases was 1.68–1.71, only slightly higher than the stoichiometric ratio for HAp. Interestingly, the addition of NaNO_2 in the present study resulted in a surface morphology similar to that observed by Ban and Maruno under a combination of high current density and high temperatures.³¹ The change in surface morphology as a result of either KCl or NaNO_2 additions to the plating bath may be associated with their effect on the activity of the calcium and phosphate ions in solution, and thus on the solubility of the CaP salt.

Figure 8 shows that all coatings are crystalline in nature and free of cracks. The high level of porosity may be related to the formation at the surface and trapping inside the deposited layer of hydrogen gas bubbles during electrodeposition. The presence of adsorbed hydrogen gas bubbles might also interfere with the deposition process, by reducing the number of sites available for deposition of CaP and affecting mass transport processes. Kumar et al. suggested that hydrogen evolution might decrease the adhesion between the CaP coating and the substrate.³⁵ On the other hand, a high level of porosity shall provide a better scaffold for integration of mineralized bone tissue, which may be even more important than the chemistry of the CaP coating per se, thus enhancing the biological fixation. It should also be recalled that the biological mineral has two major functions, mechanical and homeostatic.³⁶ Not only do the biological apatite crystals serve as a storage repository for Ca, Mg and phosphate ions, they also reinforce the collagenous matrix, providing it with high strength and rigidity also under compression. Hence, it may be anticipated that the morphology of the CaP crystals

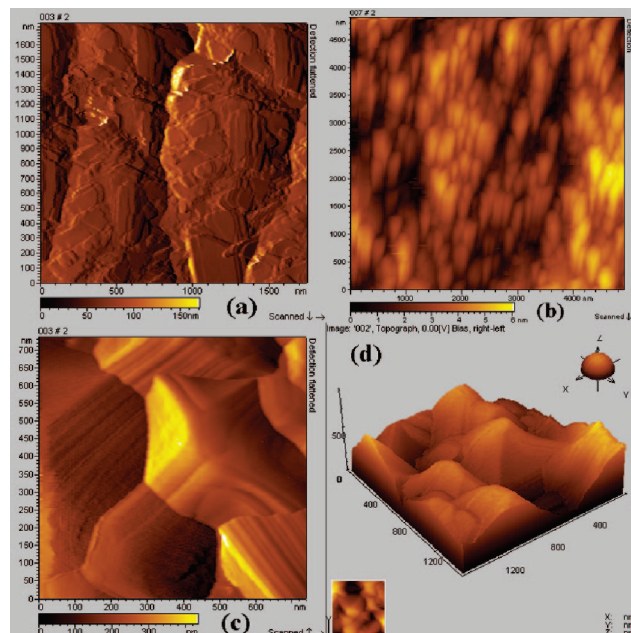


Figure 9. AFM images of the top surface of coatings produced at: (a) $\text{pH}_0 = 6.0$, $T = 90$ °C, $t = 5$ min; (b) $\text{pH}_0 = 6.0$, $T = 85$ °C, $t = 2$ h; and (c) $\text{pH}_0 = 6.0$, $T = 90$ °C, $t = 2$ h, in the presence of 0.10 M KCl. A 3D view of the latter sample is presented in (d).

would affect, among others, the mechanical properties of the bone tissue. Regarding the EDS results, all spectra contained peaks of Ca, P, O, and Ti only; in most cases, the Ca/P ratio was close to 1.67, the minimum value required by the FDA for HAp coatings.³⁷

The topography of different coatings was also evaluated by means of ex situ AFM imaging. Figure 9 shows some typical AFM images. The deflection image is more sensitive than topography images to delegate spatial information, such as sharp edges. Figure 9a shows the top surface of a coating that was deposited for 5 min only at $\text{pH}_0 = 6.0$, $T = 90$ °C. The morphology of this coating seems to be two-dimensional (2D), with platelet crystals that are smaller than 200 nm in length and width, and less than 20-nm thick (the latter dimension was determined by AFM line scans on the topography image). Similar findings have been reported for deposition at $\text{pH}_0 = 6.0$, $T = 85$ °C for either 1 or 10 min.³ Figure 9b shows the top surface of a coating that was deposited for 2 h at $\text{pH}_0 = 6.0$, $T = 85$ °C. Note that this image was acquired at a lower magnification compared to Figure 9a. Topographical bands with preferred orientation (and a columnar growth) are evident. Each band seems to be a stacking (assembly) of several rods; or, actually, hexagons. Each hexagon is approximately 137 nm in diameter. Central holes can be noticed in the center of some of these stackings. In addition, large pores are evident between the bands. The morphology of crystals that appears in Figure 9b is similar to that of HAp crystals in mature human dental enamel.³⁸ This suggests that synthetic HAp coatings formed by electrocrystallization are more biomimetic, at least with respect to their structure and morphology, compared to those currently produced by plasma spraying. Figure 9c shows the top surface of a coating that was deposited for 3 h at $\text{pH}_0 = 6.0$, $T = 90$ °C, in the presence of 0.10 M KCl. This high-magnification image is similar to those observed for 3D growth from a bath at $\text{pH}_0 = 6.0$, $T = 85$ °C for either 30 or 60 min.³ A 3D view of another zone on the same sample as in Figure 9c is presented in Figure 9d. Terraces are distinct in Figure 9c, as well as crystal

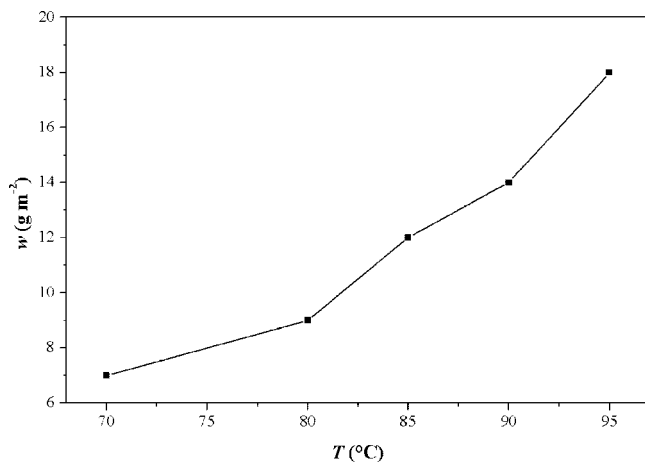


Figure 10. The dependence of the measured weight of coatings deposited at $\text{pH}_0 = 6.0$ for 3 h on the bath temperature.

growth along a preferential direction. Based on the XRD data, this direction is [002]. AFM images of coatings produced at $\text{pH}_0 = 4.2$ or in the presence of NaNO_2 are not presented here because the high level of porosity and high roughness significantly hindered the AFM tip movement.

The dependence of the measured weight of coatings deposited at $\text{pH}_0 = 6.0$ for 3 h on the bath temperature is shown in Figure 10. The coating weight is found to increase with increasing temperature. Plotting the data from Figure 10 in the form of ν versus $1/T$, where ν is the deposition rate (in units of $\text{g}(\text{h}\cdot\text{m}^2)^{-1}$) and T is the absolute temperature, the following relation is obtained:

$$\ln(\nu) = 14.74 - 4785 \frac{1}{T}, R^2 = 0.9742 \quad (21)$$

where R^2 is the determination coefficient. It should be noted that the relatively low value of R^2 results from the narrow range of temperatures (70–95 °C), based on which eq 21 was derived. This narrow temperature range was associated with the conditions under which good electrodeposits of HAp could be formed on CP-Ti from the same bath.³⁴ Comparing to Arrhenius equation

$$\nu = A^* \exp\left(-\frac{\Delta G^\ddagger}{RT}\right) \quad (22)$$

the standard enthalpy of activation is estimated to be

$$\Delta H^\ddagger \approx 40 \pm 4 \text{ kJ/mol} \quad (23)$$

In eq 22, A^* is a pre-exponential factor, R is the molar gas constant, and $\Delta G^\ddagger = \Delta H^\ddagger - T\Delta S^\ddagger$ is Gibbs energy of activation. The value of the standard enthalpy of activation given in eq 23 is similar to the values reported by other investigators for apatites growth,^{39,40} and is within the range typical of a wide variety of mineral-solution alteration processes.⁴¹ Furthermore, while it is too high for a bulk diffusion-controlled process, it is possible for reaction kinetics that is controlled by the interfacial area.⁴² This conclusion is supported by the work of Eliaz and Eliyahu, who concluded that mass transport could have only a secondary role in the deposition of HAp, based on ex situ cyclic voltammetry measurements.³

The thickness of the porous coatings was measured from metallographic cross-sections, in accordance with ASTM F 1854. The combined effect of deposition time and pH on the measured coating weight and thickness is demonstrated in Figure

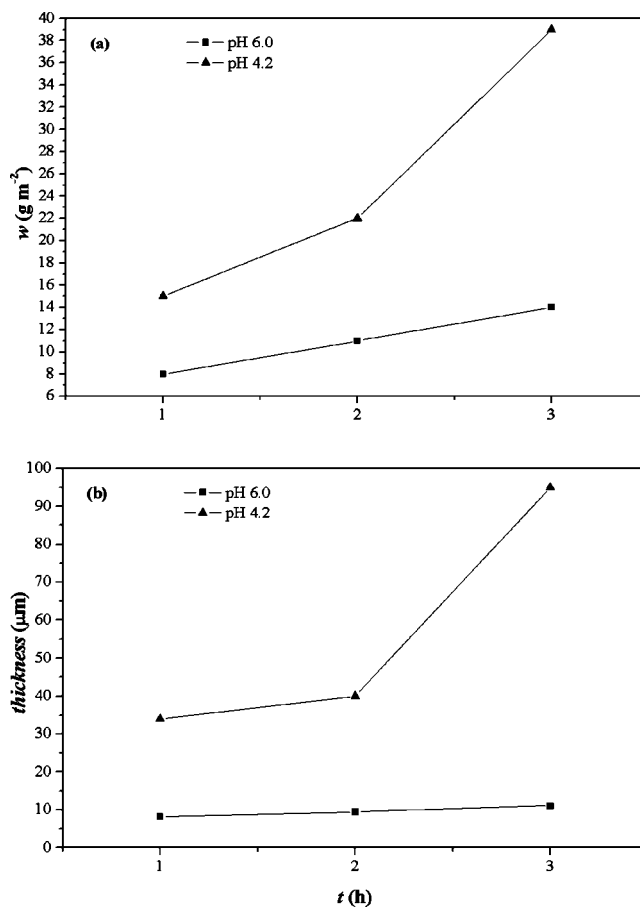


Figure 11. The dependence of the measured coating weight (a) and coating thickness (b) on the pH and deposition time. All coatings were deposited at $T = 90$ °C.

11 for coatings deposited at $T = 90$ °C. Expectedly, the mass gain increases as the deposition time is increased from 1 to 3 h (Figure 11a). Deposition at $\text{pH}_0 = 4.2$ results in a higher mass gain at any time compared to deposition at $\text{pH}_0 = 6.0$. This means that either the former are thicker, or the latter are more porous, in accordance with our XRD data (see Figure 2 and the related discussion above). Figure 11b shows the values of coating thickness, as measured microscopically (both by light microscope and by SEM). It is evident that while the thickness was increased from 8 to 11 μm as the deposition time was increased from 1 to 3 h at $\text{pH}_0 = 6.0$, the thickness was increased from 34 μm to as high as 95 μm when deposition was carried out at $\text{pH}_0 = 4.2$. The shortcoming of thickness increase, however, was decrease in the adhesion of the coating to the substrate, as evaluated by either a tape peel-off test or a scratch test. Division of the coating weight density by the coating thickness reveals that coatings deposited at $\text{pH}_0 = 4.2$ are actually more porous than coatings deposited at $\text{pH}_0 = 6.0$. This difference may be explained based on the role of the hydrogen evolution reaction, which becomes more significant in more acidic plating baths. When these bubbles are large enough, they are dislodged by buoyancy. In addition, residual stresses may also develop in the coating. Consequently, the deposition of HAp may be impeded, or weakly bonded crystals may be torn from the deposit and be released into the solution. Coatings deposited for 3 h at $\text{pH}_0 = 4.2$ were also very flaky. Therefore, and because deposition for 2 h resulted in sufficiently thick coatings, it was concluded that deposition for 2 h was optimal

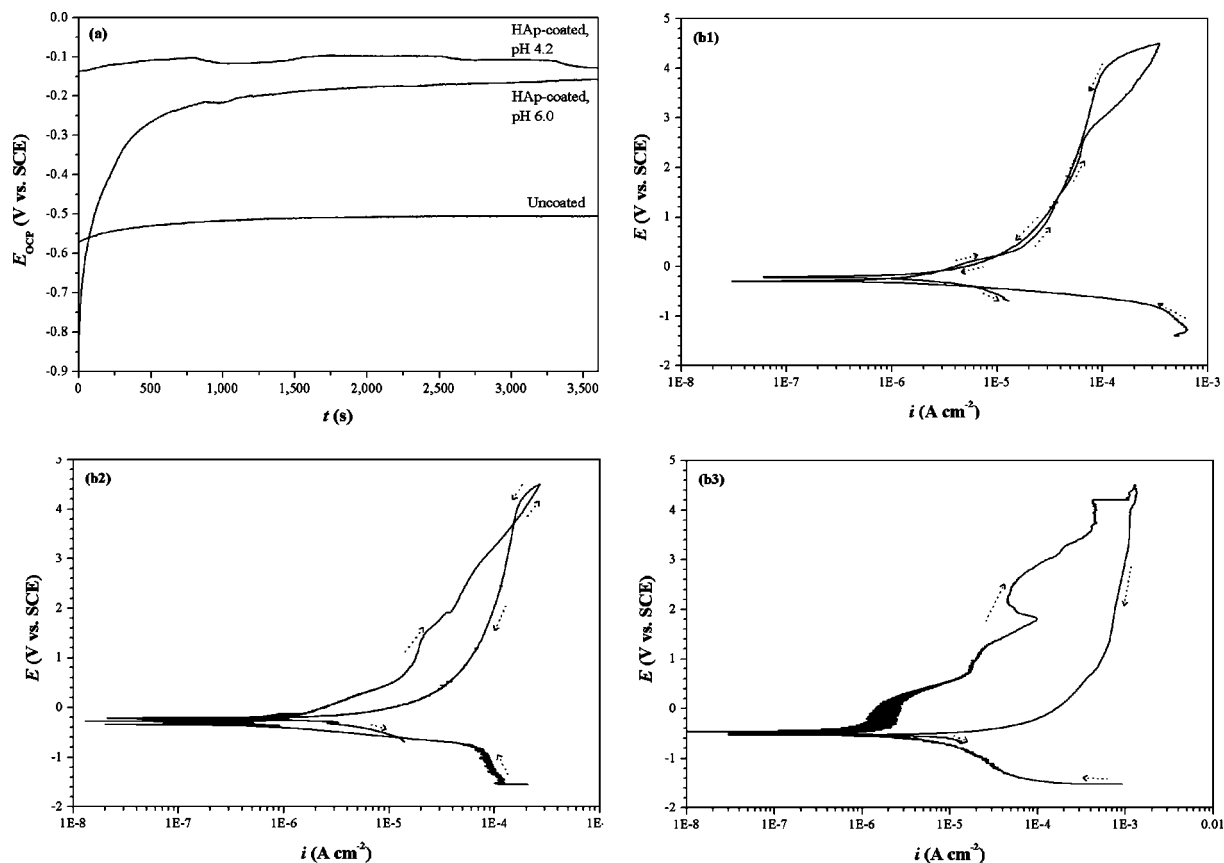


Figure 12. Corrosion measurements of uncoated and HAp-coated samples in Ringer's SBF at pH = 7.4 and $T = 37$ °C. (a) OCP vs time curves of uncoated Ti, Ti coated with HAp for 2 h at pH₀ = 6.0 and $T = 95$ °C, and Ti coated with HAp for 3 h at pH₀ = 4.2 and $T = 90$ °C. (b) Cyclic potentiodynamic polarization curves for uncoated Ti (1), Ti coated with HAp for 2 h at pH₀ = 6.0 and $T = 85$ °C (2), and Ti coated with HAp for 3 h at pH₀ = 4.2 and $T = 90$ °C (3). The dotted arrows mark the forward and backward directions of the scan.

for this bath (while deposition for 3 h was desirable in order to obtain thicker coatings at pH₀ = 6.0).

Corrosion measurements of both uncoated and coated samples were carried out in Ringer's SBF at pH = 7.4 and $T = 37 \pm 0.1$ °C. First, the OCP was monitored as a function of time for 60 min, or until E_{corr} was attained. Next, a cyclic potentiodynamic polarization scan was run. Figure 12a shows the typical OCP versus time curves of uncoated Ti, Ti coated with HAp for 2 h at pH₀ = 6.0 and $T = 95$ °C, and Ti coated with HAp for 3 h at pH₀ = 4.2 and $T = 90$ °C. The OCP was found to be shifted considerably in the positive direction due to the presence of the HAp coating on the surface, indicating that the coating provided a more noble (better corrosion resistant) surface. This shift was from -506 mV vs SCE for the uncoated sample, to -158 and -129 mV vs SCE for samples coated at pH₀ = 6.0 and pH₀ = 4.2, respectively. The slightly less negative value for the coating deposited at pH₀ = 4.2 compared to the coating deposited at pH₀ = 6.0 could be attributed to the higher thickness of the former. The high porosity of the coating deposited at pH₀ = 4.2 did not degrade the OCP vs time behavior (except of minor fluctuations in the potential values). Thus, it may be concluded that the porous HAp coatings do not stimulate underfilm corrosion within the measurement time frame.

The most useful procedure for testing susceptibility of small implants, in their final form and finish, to localized corrosion is described in ASTM F 2129. Following the guidelines of this standard, cyclic potentiodynamic polarization curves are shown in Figure 12b. In Figure 12b(1), a curve for uncoated Ti is

shown. The dotted arrows mark the forward and backward directions of the scan. The corrosion potential (E_{corr}) and corrosion current density (i_{corr}) were determined through Tafel extrapolation as -297 mV vs SCE and 1.5×10^{-6} A cm⁻², respectively. No active-to-passive transition is evident (namely, there is no primary passivation potential, E_{pp} , with the corresponding critical current density, i_{cc}). Moreover, neither breakdown (critical pitting) potential (E_b) nor protection potential (E_p) is evident, indicating that the material is covered with a protective oxide layer. The absence of a hysteresis loop when scanning backward is indicative of repassivation. Thus, it may be concluded that the uncoated CP-Ti has good resistance against localized corrosion (either pitting or crevice). This typical corrosion behavior of Ti and its alloys in SBFs has commonly been documented.^{43,44}

A cyclic potentiodynamic polarization curve for Ti coated with HAp for 2 h at pH₀ = 6.0 and $T = 85$ °C is shown in Figure 12b(2). Again, neither an active-to-passive transition nor a hysteresis loop is evident. On the basis of Tafel extrapolation, the values of E_{corr} and i_{corr} are -362 mV vs SCE and 7×10^{-7} A cm⁻², respectively. The lower value of i_{corr} compared to that for the uncoated sample should result in a lower corrosion rate of the coated sample. Thus, it may be concluded that although the HAp coating is porous and the base metal is naturally passive, the coating does not have a detrimental effect on the corrosion resistance. It should be noted that, following the cyclic potentiodynamic polarization tests, visual inspection was carried out. Neither physical detachment of the coating from the substrate nor a change

in the color of the solution was evident. A cyclic potentiodynamic polarization curve for Ti coated with HAp for 3 h at $\text{pH}_0 = 4.2$ and $T = 90^\circ\text{C}$ is shown in Figure 12b(3). In this case, instead of a good repassivation behavior, the backward scan demonstrates a large hysteresis loop, with no protection potential. In addition, no well-defined passivation region is evident in the forward scan. Based on Tafel extrapolation, the values of E_{corr} and i_{corr} are -381 mV vs SCE and $5.9 \times 10^{-6}\text{ A cm}^{-2}$, respectively. Both the lowest corrosion potential and the highest corrosion current density indicate that the corrosion performance of this coated sample is inferior compared to the former two samples. It is likely that the very porous coating interrupted the oxide layer growth and triggered localized (e.g., pitting) and/or underfilm corrosion. Therefore, at least from corrosion resistance standpoint, HAp coatings deposited at $\text{pH}_0 = 6.0$ are preferable.

4. Conclusions

In this work, HAp was deposited electrochemically on CP-Ti from solutions containing $\text{Ca}(\text{NO}_3)_2$ and $\text{NH}_4\text{H}_2\text{PO}_4$, at either $\text{pH}_0 = 6.0$ or $\text{pH}_0 = 4.2$. The effects of bath composition, pH, temperature and deposition time were studied. The current density transients during deposition were much different when the pH was 4.2 than when it was 6.0. Coatings deposited at $\text{pH}_0 = 4.2$ were thicker, less crystallized and more porous than coatings deposited at $\text{pH}_0 = 6.0$, and also revealed traces of OCP (and, possibly, of DCPA) as well as a different surface morphology. The content of OCP in coatings deposited at $\text{pH}_0 = 4.2$ was decreased as a result of increasing the bath temperature. Texture (preferred orientation) of HAp was observed, both at $\text{pH}_0 = 4.2$ and at $\text{pH}_0 = 6.0$. The morphology of the crystals was either plate-like (bar) or platelet. Similarity was observed, already on the nanoscale, to the morphology of HAp crystals in mature human dental enamel. The coating weight and thickness were found to increase with increasing bath temperature. The standard enthalpy of activation was $\sim 40\text{ kJ mol}^{-1}$, which excludes bulk diffusion-controlled processes from being rate determining. The samples coated with HAp at $\text{pH}_0 = 6.0$ exhibited a better corrosion resistance behavior, thus indicating the formation of a stable HAp/Ti interface. On the other hand, the high porosity in the coatings deposited at $\text{pH}_0 = 4.2$ had a detrimental effect on the corrosion behavior. The addition of KCl to the bath resulted in the formation of Ca-enriched, thicker coatings, with a different surface morphology of needles. The addition of NaNO_2 also resulted in thicker coatings, but with a less pronounced preferred orientation and a dendritic surface morphology. Speciation-precipitation calculations were made in order to better understand the thermodynamic driving forces. The ability to modify the chemistry and surface morphology of the coating by fine control of bath composition, pH and temperature makes electrochemical deposition a versatile process for deposition of coatings on implants, with a tailored body response.

Acknowledgment. The authors thank Z. Barkay and Y. Rosenberg from the Wolfson Applied Materials Research Centre at Tel-Aviv University for their help in SEM and XRD tests, respectively. The assistance of M. Eliyahu in the AFM work is acknowledged. N.E. thanks the Dan David and Ella Kodesh Foundations for their financial support. T.M.S. acknowledges

Pikovsky Valachi Foundation, Tel-Aviv University, for providing him with a postdoctoral scholarship.

References

- (1) Hacking, S. A.; Tanzer, M.; Harvey, E. J.; Krygier, J. J.; Bobyn, J. D. *Clin. Orthop. Rel. Res.* **2002**, *405*, 24–38.
- (2) Brown, P. W. *J. Am. Ceram. Soc.* **1992**, *75*, 17–22.
- (3) Eliaz, N.; Eliyahu, M. *J. Biomed. Mater. Res. A* **2007**, *80*, 621–634.
- (4) Cullity, B. D.; Stock, S. R. *Elements of X-Ray Diffraction*, 3rd ed.; Prentice Hall: Upper Saddle River, NJ, 2001; pp 279, 292, 402.
- (5) Vijayaraghavan, T. V.; Benesalem, A. *J. Mater. Sci. Lett.* **1994**, *13*, 1782–1785.
- (6) Manso, M.; Jiménez, C.; Morant, C.; Herrero, P.; Martínez-Duart, J. M. *Biomaterials* **2000**, *21*, 1755–1761.
- (7) Le Geros, R. Z. *Calcium Phosphates in Oral Biology and Medicine. Monograph in Oral Science*; Karger: Basel, 1991.
- (8) Wang, H.; Eliaz, N.; Xiang, Z.; Hsu, H. P.; Spector, M.; Hobbs, L. W. *Biomaterials* **2006**, *27*, 4192–4203.
- (9) Eliaz, N.; Kopelovitch, W.; Burstein, L.; Kobayashi, E.; Hanawa, T. *J. Biomed. Mater. Res. A*, DOI 10.1002/jbm.a.32129.
- (10) Müller, B. *Manual of ChemEQL*, (Version 3.0); Limnological Research Center EAWAG/ETH: Kastanienbaum, Switzerland 2004.
- (11) Loewenthal, R. E.; Ekama, G. A.; Marais, G. V. R. *Water SA* **1989**, *15*, 3–24.
- (12) Sillén, L. R.; Martell, A. E. *Stability Constants of Metal-Ion Complexes*; The Chemical Society: London, 1964; Supplement 17, pp180–181.
- (13) Koutsoukos, P.; Amjad, Z.; Tomson, M. B.; Nancollas, G. H. *J. Am. Chem. Soc.* **1980**, *102*, 1553–1557.
- (14) Benefield, L. D.; Judkins, J. F.; Weand, B. L. *Process Chemistry for Water and Wastewater Treatment*; Prentice-Hall: Englewood Cliffs, NJ, 1982.
- (15) Marczewski A. W. <http://hermes.umcs.lublin.pl/~awmarcz/awm/utills/Activity.htm>.
- (16) Parkhurst, D. L.; Appelo, C. A. J. *User's Guide to PHREEQC (Version 2) - A Computer Program for Speciation, Batch-Reaction, One-Dimensional Transport, and Inverse Geochemical Calculations. Water-Resources Investigations Report 99-4259*; U.S. Department of the Interior, U.S. Geological Survey, Denver, CO, 1999.
- (17) Song, Y.; Hahn, H. H.; Hoffmann, E. *Chemosphere* **2002**, *48*, 1029–1034.
- (18) Song, Y.; Weidler, P. G.; Berg, U.; Nüesch, R.; Donnert, D. *Chemosphere* **2006**, *63*, 236–243.
- (19) Sinitsyna, O. V.; Veresov, A. G.; Kovaleva, E. S.; Kolen'ko, Yu. V.; Putlyayev, V. I.; Tretyakova, Yu. D. *Russ. Chem. Bull., Int. Ed.* **2005**, *54*, 79–86.
- (20) van der Houwen, J. A. M.; Valsami-Jones, E. *Env. Techn.* **2001**, *22*, 1325–1335.
- (21) Plant, L. J.; House, W. A. *Colloids and Surfaces A: Physicochem. Eng. Aspects* **2002**, *203*, 143–153.
- (22) Jeffree, R. A.; Markich, S. J.; Brown, P. L. *Aust. J. Mar. Freshwater Res.* **1993**, *44*, 609–634.
- (23) Tung, M. S.; Eidelman, N.; Sieck, B.; Brown, W. E. *J. Res. Natl. Bur. Stand.* **1988**, *93*, 613–624.
- (24) Abbona, F.; Lundager Madsen, H. E.; Boistelle, R. *J. Cryst. Growth* **1986**, *74*, 581–590.
- (25) Ferreira, A.; Oliveira, C.; Rocha, F. *J. Cryst. Growth* **2003**, *252*, 599–611.
- (26) Oliveira, C.; Georgieva, P.; Rocha, F.; Ferreira, A.; de Azevedo, S. F. *J. Cryst. Growth* **2007**, *305*, 201–210.
- (27) Abbona, F.; Christensson, F.; Franchini Angela, M.; Lundager Madsen, H. E. *J. Cryst. Growth* **1993**, *131*, 331–346.
- (28) LeGeros, R. Z. In *Hydroxyapatite and Related Materials*; Brown, P. W., Constantz B., Eds.; CRC Press: FL, 1994; pp 3–28.
- (29) Shirkhanzadeh, M. *J. Mater. Sci.: Mater. Med.* **1998**, *9*, 67–72.
- (30) Zhang, Y.; Lu, J. *Nanotechnology* **2008**, *19*, 155608.
- (31) Ban, S.; Maruno, S. *Biomaterials* **1998**, *19*, 1245–1253.
- (32) Doi, Y.; Eanes, E. D. *Calcif. Tissue Int.* **1984**, *36*, 39–47.
- (33) Jinawath, S.; Pongkao, D.; Suchanek, W.; Yoshimura, M. *Int. J. Inorg. Mater.* **2001**, *3*, 997–1001.
- (34) Eliaz, N.; Sridhar, T. M.; Rosenberg, Yu. In *Proceedings of the 10th World Conference on Titanium*; Lütjering, G., Albrecht, J., Eds.; Wiley-VCH: Weinheim, Germany, 2004; Vol. 5, pp 3299–3306.
- (35) Kumar, M.; Dasarathy, H.; Riley, C. *J. Biomed. Mater. Res.* **1999**, *45*, 302–310.
- (36) Boskey, A. L. *J. Musculoskel. Neuron Interact.* **2002**, *2*, 532–534.

- (37) Callahan, T. J.; Gantenberg, J. B.; Sands, B. E. In *ASTM STP 1196: Characterization and Performance of Calcium Phosphate Coatings for Implants*; Horowitz, E., Parr, J. E., Eds.; ASTM: PA, 1994; pp 185–197.
- (38) Robinson, C.; Connell, S.; Kirkham, J.; Shore, R.; Smith, A. *J. Mater. Chem.* **2004**, *14*, 2242–2248.
- (39) Ban, S. *Dental Mater. J.* **2003**, *22*, 467–474.
- (40) Tanahashi, M.; Kokubo, T.; Matsuda, T. *J. Biomed. Mater. Res.* **1996**, *31*, 243–249.
- (41) Lasaga, A. C. *Kinetic Theory in the Earth Sciences*; Princeton University Press: NJ, 1997.
- (42) Laidler, K. J. *Chemical Kinetics*; McGraw-Hill: New York, 1958.
- (43) Eliaz, N. In *Corrosion Science and Technology: Mechanism, Mitigation and Monitoring*; Kamachi Mudali, U., Baldev, R., Eds.; Narosa Publishing House: New Delhi, 2008; Chapter 12, pp 356–397.
- (44) Eliaz, N.; Sridhar, T. M.; Kamachi Mudali, U.; Baldev, R. *Surf. Eng.* **2005**, *21*, 238–242.

CG800016H